Cooper et al. (2016)
Aridity-induced Miocene canyon incision in the Central Andes
GSA Data Repository

DR1. Sample descriptions

Nine hematite-bearing samples were collected from three vertical drill holes in the Cerro Colorado copper mine, northern Chile (Fig. DR1.1). The samples were all composed of highly-altered porphyritic quartz monzonite, in which the primary igneous assemblage had been largely replaced by sericite and clay. The samples were cross-cut by a network of mm- to cm-wide veins of hematite, often accompanied by quartz, and occasionally by minor goethite or Cu oxide (Fig. DR1.2).

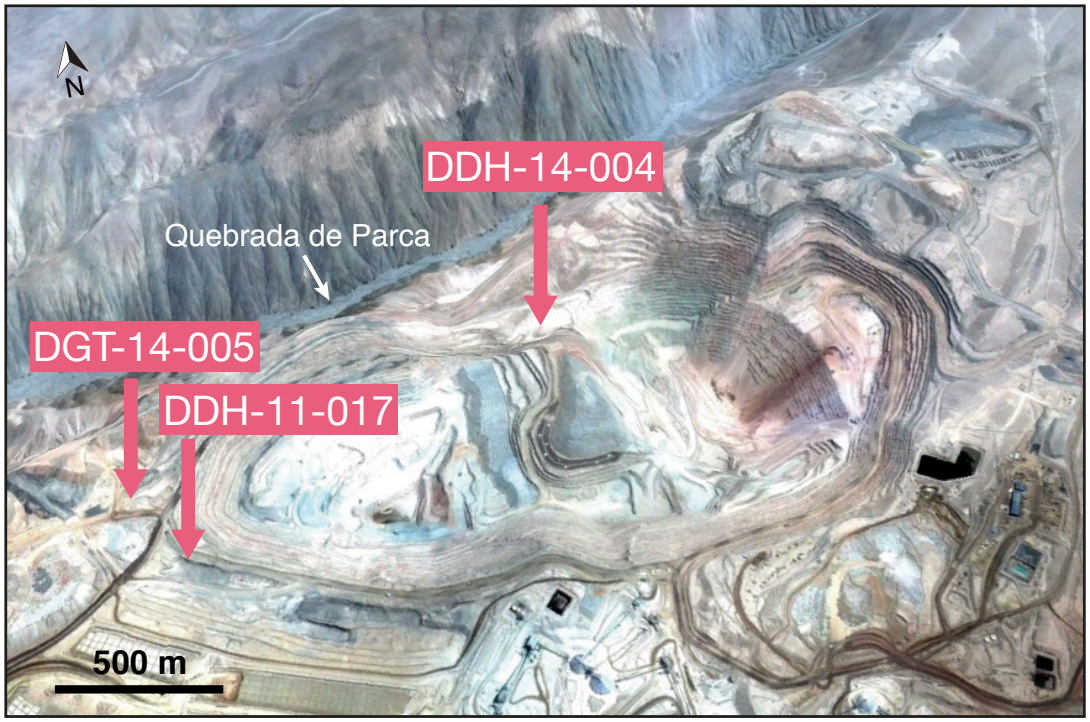

Figure DR1.1. An oblique Google Earth™ view of Cerro Colorado mine showing the locations of the sampled drill holes. The Quebrada Parca canyon can be clearly seen running E-W along the northern edge of the pit.

DR2. (U-Th)/He hematite analysis

DR2.1 Methodology

Samples were crushed into <0.5 mm diameter chips, and pure fragments of hematite with no adhering material (e.g. quartz, mica, clays) were selected for analysis. Representative chips from each sample are shown in Figure DR1.2. Because the chips were internal fragments of larger hematite pieces, we did not need to correct for alpha ejection. However, careful photographs of the chips were taken and measured to estimate their volumes (Table DR5).

Chips were loaded into individual platinum (Pt) microcrucibles, which were crimped closed and loaded into the sample holder of the laser chamber of the Quadrupole Isotope Dilution extraction line at the Caltech Noble Gas Laboratory. The laser chamber was pumped down to ultra-high vacuum overnight and the helium was extracted from each sample using a 75 Watt, 976 nm near infra-red diode laser. Samples were heated to ~950˚C for 4 minutes and temperature was carefully tracked with a calibrated optical pyrometer. This comparatively low extraction temperature was adopted to avoid problems with U volatilization that has been observed in goethite at temperatures >1000°C (Vasconcelos et al., 2013). The evolved ^{4}He gas first passed

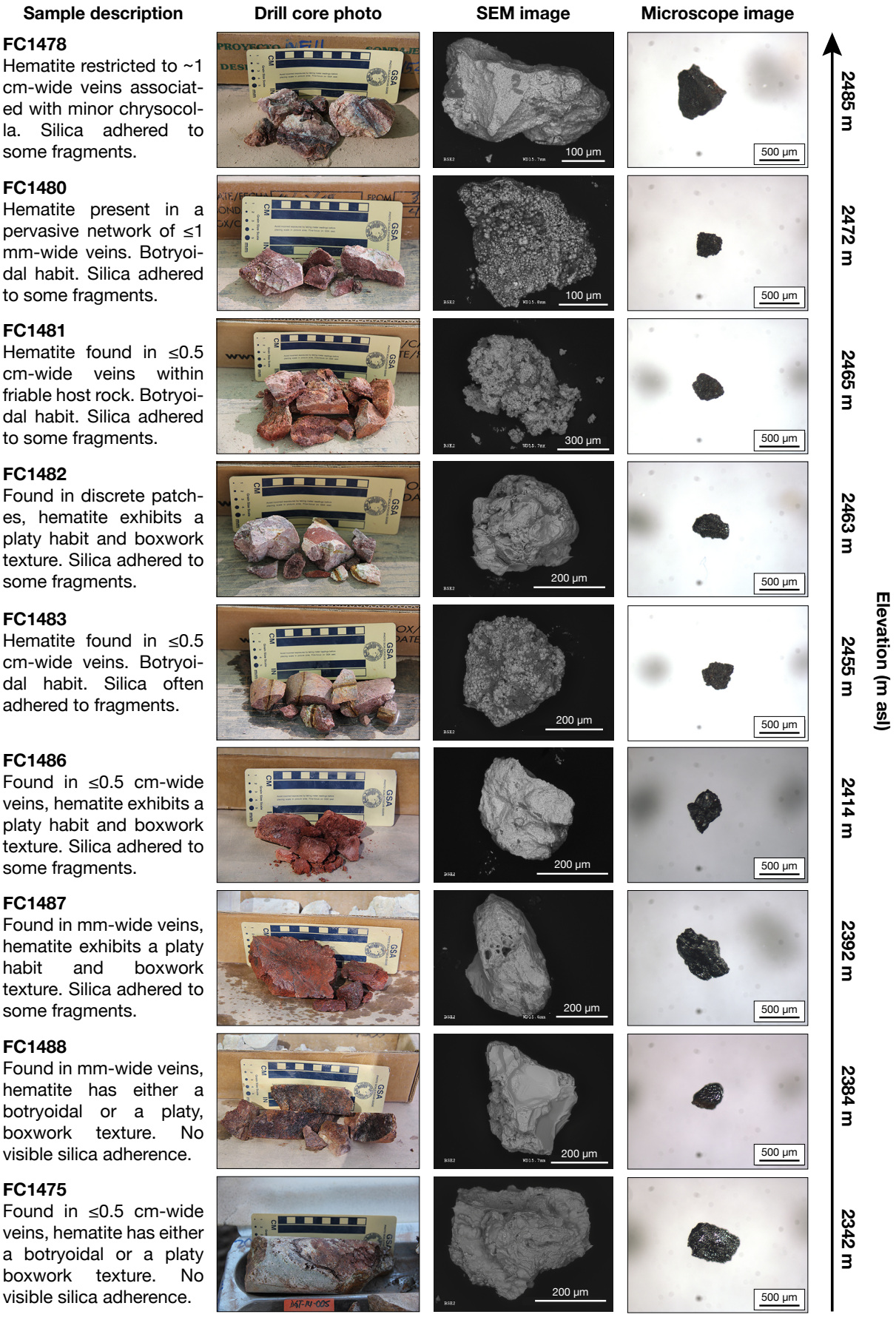

Figure DR1.2. Drill core photographs, SEM images, and microscope images of hematite vein material analysed in this study. Samples are shown in order of elevation.

through a liquid nitrogen trap with activated charcoal and then was spiked with ^{3}He and cryo-focused on a charcoal-bearing cold head at 14K. Helium was released by warming to 36K and analyzed on a Balzers Prisma QMS 200 quadrupole equipped with a Channeltron electron multiplier detector, which contains a room temperature SAES NP-10 in the analysis chamber. To ensure complete helium extraction, every sample was analyzed a second time after being heated to ~960°C. Between sample analyses, a known ^{4}He aliquot was spiked with ^{3}He and analyzed to allow the amount of unknown ^{4}He in the sample to be calculated. In addition to the samples, empty Pt tubes were analyzed as blanks.

After ^{4}He analysis the samples were unloaded from the laser chamber and dissolved for U and Th analysis. Pt packets containing hematite chips were placed individually in Teflon vials with ~1 mL concentrated hydrochloric acid (HCl), capped, and placed on a hot plate at ~140˚C for 12 hours to fully dissolve the hematite. Because the chips were not removed from the Pt carriers prior to dissolution, it was not possible to visually confirm complete dissolution. Instead, separate aliquots of each sample were placed in a Teflon vial and subjected to the same acid treatment. After 12 hours, no solids remained from any sample. After dissolution, the sample vials were opened and allowed to dry out. The precipitates were re-dissolved in 50 µL of nitric acid (HNO_3), spiked with a precise amount of ^{235}U and ^{230}Th for isotope dilution, and diluted with 1 mL of deionized water. The sample solutions were analyzed on an Agilent Technologies 8800 ICP-MS.

The He, U, and Th data were used to calculate raw ages using an iterative approach to the (U-Th)/He age equation. Within this calculation, the concentration of ^{235}U was derived from the measured ^{238}U concentration using the known ratio of these isotopes in nature. Analytical errors were propagated through the age calculation.

DR2.2 (U-Th)/He age variations at a given stratigraphic position: Potential causes and data treatment

Figure 2 shows that hematite (U-Th)/He ages at a given stratigraphic position vary outside the analytical uncertainty of ~10% (2σ). As noted in the main text, this range in ages may arise from a prolonged period of hematite growth at any given stratigraphic depth. Such prolonged growth is not unusual, and goethite ages from single hand samples have been seen to vary by many millions of years because the process of mineralization is ongoing (e.g. Heim et al., 2006; Vasconcelos et al., 2013). However, we cannot rule out possible analytical issues that are not captured in our uncertainty estimates as an additional source of stratigraphic age variability. Similarly, 4 of our samples give ages that are obviously too old, unambiguously demonstrating a presently unidentified problem or problems.

Likely candidates for hematite age variability and/or anomalously old ages are mentioned below for completeness. While these issues may have affected the data to a greater or lesser degree, the compelling correlation in Figure 2 cannot arise from such factors.

Possible sources of anomalous hematite He ages are:

1) Contamination of hematites with U- and Th-bearing mineral inclusions yielding anomalously old ages, both because the inclusions may predate hematite mineralization, and in some cases may not be dissolved in our HCl dissolution technique. A likely candidate for problematic inclusions is zircons from the original igneous body. While SEM and thin-section optical microscopy showed only silica adhering to hematites, such analyses are impossible on grains subjected to He dating.
2) Overly aggressive heating of goethite during He degassing volatilizes U and thereby causes anomalously old He ages (e.g. Vasconcelos et al., 2013). Because a similar effect may occur in hematite, we used a comparatively low degassing temperature of ~950°C. In a system in which Th/U is uniform, U volatilization and associated old He ages can be recognized (Vasconcelos et al., 2013). However, the hematites in the present study vary greatly in Th/U, with no indication that older ages correlate with high Th/U. As a result, we cannot rule out this effect as a cause of the anomalously old ages and possibly as a cause of some of the age variation within the bulk of the samples.
3) The dated hematites are large enough that α ejection is not expected to be a major factor. However, redistribution of α particles may occur if U and Th are highly zoned. We have no data from which to evaluate this possibility, though it seems unlikely to be a major factor and would not likely yield the occasional extremely old ages we observe.

DR3. Channel profile analysis

Steady-state longitudinal channel profiles typically follow a power law relationship between local channel slope (S) (m/m) and drainage area (A) (m^2) (e.g. Hack, 1957; Flint, 1974; Tarboton et al., 1989):

$$S = k_s A^{-\theta} \quad (1)$$

where k_s ($m^{2\theta}$) is the channel steepness, a measure of local channel slope adjusted for the upstream increase in drainage area, and θ (dimensionless) is the channel concavity. In our study, we used $\theta = 0.46$, which adequately described the concavity of the Quebrada de Parca river from regressions of slope-area data.

Linearized channel profiles were created by replacing profile distance (x) with the integral of the upstream accumulation area, χ (Perron and Royden, 2013):

$$z(x) = z(x_b) + k_s \chi \quad (2)$$

where $z(x_b)$ is elevation at the river base level. Eq. 2 shows that the channel steepness (k_s) sets the slope of the linearized channel profile.

DR4. Surface uplift calculations

To calculate the magnitude of surface uplift (ΔZ), we first reconstructed the linearized channel profile of the Quebrada de Parca river prior to uplift, and then calculated the difference in base level elevation between the paleo-river and the modern river (e.g. Adams et al., 2016). The base level of the paleo-river was constrained using a linear least-squares regression protocol between elevation and χ values from the preserved, low-channel steepness segment of the river that existed prior to uplift (Fig. DR3). Because the errors on the elevation and χ data are minimal, we estimated the uncertainty in our projections based on the variation in elevation and χ data along the fitted segment. For this we used a jackknife $N - d$ protocol, where N is the number of data pairs in the preserved river segment and d is a number less than N. In order to provide a robust assessment of the scatter in our data we performed 10,000 linear regressions with $\sqrt{N}$ randomly-selected data pairs from the preserved river segment. Reconstructed base level elevations are reported as the mean of 10,000 y-intercept values, and the uncertainty is reported as 2 standard deviations on the mean. We performed this analysis on the Quebrada de Parca (Fig. 3 and Fig. DR3) and a neighboring fluvial system to the south, the Quebrada de Tambillo (see Fig. 1 for locations), to demonstrate that the Quebrada de Parca is not a regional anomaly. The extent of the upper projected reach was determined by the maximum extent of a consistent channel steepness (i.e. linear segment) directly upstream of the major convex knickpoint.

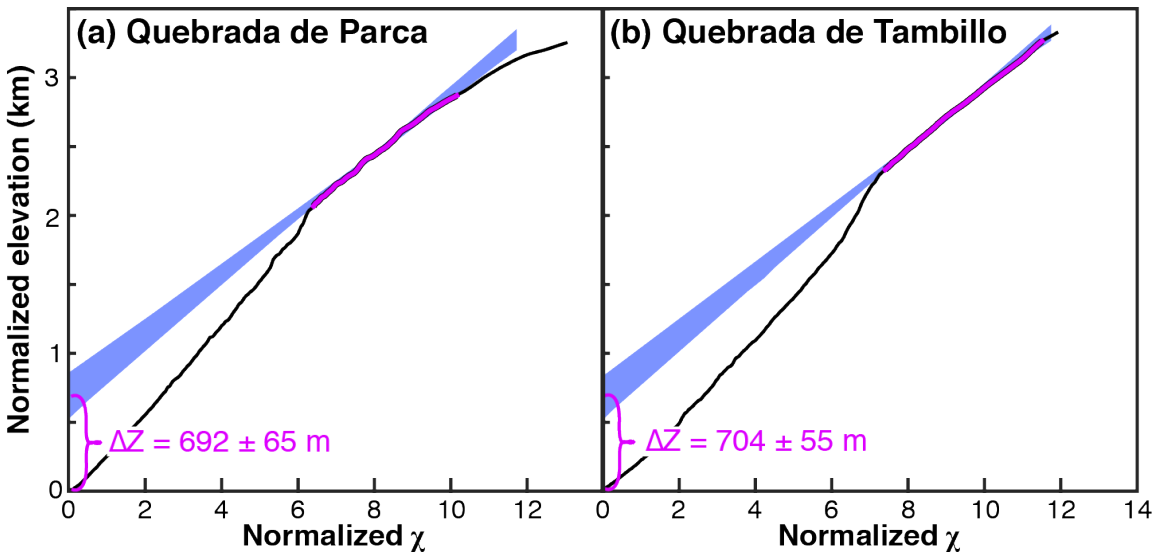

Figure DR4. Magnitudes of surface uplift (ΔZ) calculated from linearized channel profiles (black lines, hillslopes excluded). Elevation and χ are normalized to the local base level of the fluvial system in the Central Depression (~1100 m a.s.l.). The magnitude of surface uplift is determined by projecting the older, low-channel steepness segment of the river (pink) towards the local base level. Minor variations in slope within the river segment result in a range of y-intercepts values, from which a mean elevation is calculated. Surface uplift magnitudes are reported as the mean ± 2 standard deviations of the 10,000 jackknife simulations (blue lines).

DR5. Landscape evolution modeling

DR5.1. Model Formulation

In order to visualize the fluvial adjustment to changes in tectonic or climate forcing, we carried out a series of landscape evolution experiments using the Channel Hillslope Integrated Landscape Development (CHILD) landscape evolution model (Tucker et al., 2001), which tracks the evolution of surface elevations using the conservation of mass:

$$\frac{dz(x,y)}{dt} = U(x,y) - I(x,y) \quad (3)$$

where *z(x,y)*, *U(x,y)*, and *I(x,y)* are the spatial patterns of elevation (m), rock uplift rate relative to base level (m/yr), and fluvial incision rate (m/yr) (defined as positive downward). In our experiments, bedrock incision, *I*, was computed using the commonly-employed stream power incision model (e.g. Howard and Kerby, 1983; Whipple and Tucker, 1999):

$$I = KQ^m S^n \quad (4)$$

where *K* is the bedrock erodibility coefficient held fixed at $5e^{-6}$ ($1/m^{0.5}yr^{0.5}$), *Q* is the discharge (m^3/yr), *S* is the local channel slope (m/m), and *m* and *n* are dimensionless constants held fixed at 0.5 and 1, respectively. An *m*/*n* ratio of 0.5 is consistent with river incision models and observed steady-state channel concavity in other studies around the world, which typically range from 0.4 to 0.6 (Whipple and Tucker, 1999).

DR5.2. Experiment setup

Experiments were performed on a 30 x 30 km, regular triangular lattice of 250 m node spacing, with a southern open boundary. Changes in rock uplift rate and precipitation were imposed upon a steady-state landscape. To create the initial landscape, we assumed a uniform regional rock uplift rate (1 mm/yr), a mean annual precipitation rate (1 m/yr), and a random topography described by a mean elevation of 10 m and a standard deviation of 0.5 m. We then allowed the landscape to evolve until a steady-state topography associated with uniform channel steepness and incision rate was reached.

In the first scenario (Scenario 1), we imposed a linear increase in rock uplift rate in the upstream direction, whereby the rate at the drainage divide was twice that at the mouth (i.e. a linear gradient from 1 to 2 mm/yr along the 30 km model domain) (Fig. 4a). In this scenario, the mean annual precipitation rate was the same as the initial conditions (1 m/yr). This spatial pattern is consistent with the differential uplift model proposed by Isacks (1988). In the second scenario (Scenario 2), we halved the mean annual precipitation rate (0.5 m/yr) uniformly across the model to simulate a regional drying of the climate (Fig. 4b), but the rock uplift rate remained the same as the initial conditions (1 mm/yr).

DR5.3 Experiment output

To further illustrate the landscape evolution observations discussed in the main text, we have provided 4 short videos from our modeling results. All videos represent 2 Myr of landscape evolution and each time step represents 50 kyr.

- Cooper_DR5.3_scenario1_DEM.avi shows the topographic evolution of the entire landscape responding to a linear increase in rock uplift rate.
- Cooper_DR5.3_scenario1_profiles.avi shows an animated version of Fig. 4a, where river profiles respond to a linear increase in rock uplift rate.
- Cooper_DR5.3_scenario2_DEM.avi shows the topographic evolution of the entire landscape to a reduction in mean annual precipitation.
- Cooper_DR5.3_scenario2_profiles.avi shows an animated version of Fig. 4b, where river profiles respond to a reduction in mean annual precipitation.

References

Adams, B. A., Whipple, K. X., Hodges, K. V., and Heimsath, A. M., 2016, In-situ development of high-elevation, low-relief landscapes via duplex deformation in the Eastern Himalayan hinterland: Journal of Geophysical Research - Earth Surface, v. 121, p. 294−319, doi: 10.1002/2015JF003508.

Flint, J. J., 1974, Stream gradient function of order, magnitude, and discharge: Water Resources Research, v. 10, no. 5, p. 969−973.

Hack, J. T., 1957, Studies of longitudinal stream profiles in Virginia and Maryland: U.S. Geological Survey Professional Paper 294-B, p. 97.

Heim, J. A., Vasconcelos, P. M., Shuster, D. L., Farley, K. A., and Broadbent, G., 2006, Dating paleochannel iron ore by (U-Th)/He analysis of supergene goethite, Hamersley province, Australia: Geology, v. 34, no. 3, p. 173−176, doi: 10.1130/G22003.1.

Howard, A. D., and Kerby, G., 1983, Channel changes in badlands: Geological Society of America Bulletin, v. 94, no. 6, p. 739−752.

Isacks, B. L., 1988, Uplift of the Central Andean Plateau and Bending of the Bolivian Orocline: Journal of Geophysical Research, v. 93, no. B4, p. 3211−3231.

Perron, J. T., and Royden, L., 2013, An integral approach to bedrock river profile analysis: Earth Surface Processes and Landforms, v. 38, p. 570−576, doi: 10.1002/esp.3302.

Tarboton, D. G., Bras, R. L., and Rodriguez-Iturbe, I., 1989, Scaling and elevation in river networks: Water Resources Research, v. 25, p. 2037−2051.

Tucker, G. E., Lancaster, S. T., Gasparini, N. M., Bras, R. L., and Rybarczyk, S. M., 2001, An object-oriented framework for distributed hydrologic and geomorphic modeling using triangulated irregular networks: Computers & Geosciences, v. 27, no. 8, p. 959−973, doi: 10.1016/S0098-3004(00)00134-5.

Vasconcelos, P. M., Heim, J. A., Farley, K. A., Monteiro, H., and Waltenberg, K., 2013, $^{40}Ar/^{39}Ar$ and (U-Th)/He − $^{4}He/^{3}He$ geochronology of landscape evolution and channel iron deposit genesis at Lynn Peak, Western Australia: Geochimica Cosmochimica Acta, v. 117, p. 283−312, doi: 10.1016/j.gca.2013.03.037.

Whipple, K. X., and Tucker, G. E., 1999, Dynamics of the stream-power river incision model: Implications for height limits of mountain ranges, landscape response timescales, and research needs: Journal of Geophysical Research, v. 104, no. B8, p. 17,661−617,674, doi: 10.1029/1999JB900120.